arXiv:2211.12272v2 [cond-mat.soft] 14 Dec 2022

S-shaped flow curves and local stress oscillations in confined shear thickening suspensions

Haitao Hu,[1] Yiqiu Zhao,[1] Weiwei Zhao,[1] and Qin Xu[1,*]

[1] *Department of Physics, The Hong Kong University of Science and Technology, Hong Kong, China*

(Dated: December 15, 2022)

We experimentally investigated the role of boundary confinements in shear thickening suspensions. Unexpected rheological responses were observed across multiple length scales under highly confined geometries. The flow curves were found to equilibrate at very slow rates, and appeared S-shaped in steady states. By combining shear rheological characterizations with boundary stress microscopy (BSM), we observed sustained local stress oscillations in confined suspensions. The stress heterogeneities were induced by concentrated high-stress clusters that traveled stably along the flow direction. We show that the growth and relaxation of these particle clusters contributed to the non-monotonic flow curves, and mitigated the fluctuations of global shear rate. By comparing the flow properties under different system sizes, we uncovered how boundary confinements effectively determined both the rheological and statistical responses of dense suspensions to shear thickening transition.

I. INTRODUCTION

Dense granular suspensions are made of concentrated solid grains mixed with a liquid solvent. They are omnipresent in nature and industry, including mudflows in landslides [1], construction materials [2], and field-responsive fluids [3, 4]. Unlike Newtonian fluids, the rheological response of dense suspensions to shear is often nonlinear. When suspension viscosity increases with shear stress or shear rate, the flow behavior is referred to as shear thickening [5–7].

The mechanisms of shear thickening can be understood across various length scales. In recent studies, shear thickening in non-Brownian suspensions has been interpreted as a transition from an unconstrained lubricated state to a constrained frictional state [8–10]. The suspended particles form direct contacts by overcoming an intrinsic repulsive stress that often relies on the physicochemical details between particle surfaces [11, 12]. The strengthening of large-scale contact networks under shear can lead to a significant increase in flow resistance [13, 14]. This phenomenological framework not only captures the shear thickening rheology of dense suspensions [11] but also predicts the presence of S-shaped flow curves when particle volume fraction is above a critical jamming point [8, 15]. However, these non-monotonic flow curves have been rarely observed in steady state measurements [16]. Instead, unstable flow instabilities and significant stress fluctuations are commonly detected near discontinuous shear thickening transitions [17–20].

Besides the contact networks formed inside dense suspensions, flow interactions at shear boundaries also play critical roles in controlling the shear thickening strength. Similar to dry granular materials, dense suspensions tend to dilate against flow boundaries under shear [21, 22], such that the frustrated dilation gives rise to a positive normal stress [11, 23]. When shear plates are allowed to freely move by maintaining a zero normal stress, shear thickening disappears [21]. Other experiments have shown that the statistical properties of dense suspensions, including temporal stress fluctuations and local flow instabilities, can be altered by imposing different shear geometries [17, 24–26]. However, despite all these experimental implications, it remains unclear whether boundary confinements will affect the underlying shear thickening mechanisms.

To address these issues, we systematically studied the flow rheology and statistical properties of dense suspensions under different confinement conditions in this work. Combining rheological characterizations with boundary stress measurements, we observed S-shaped flow curves in steady states associated with significant local stress oscillations in highly confined suspensions. These flow features are in sharp contrast to the rheology of unconfined suspensions. Our experiments show how boundary confinements dynamically regulate frictional contact networks developed in the bulk of dense suspensions, and thus quantitatively control both the global rheology and local flow heterogeneities during shear thickening transitions.

II. STEADY STATE RHEOLOGY OF DENSE SUSPENSIONS

The dense granular suspensions were prepared by mixing the glass beads with an average diameter $d = 43 \pm 5\ \mu m$ (Sigma-Aldrich) in 20 cSt silicone oil with a high particle volume fraction $\phi = 52\%$. The shear rheology of dense suspensions was experimentally characterized by an Anton Paar MCR 302 rheometer equipped with a 43-mm-diameter parallel-plate shear cell. For a given shear rate $\dot{\gamma}$, the shear plate measures shear stress τ, and viscosity can be calculated as $\eta = \tau/\dot{\gamma}$. The gap size between the two plates was varied systematically from $h = 0.32$ mm to 1.81 mm to impose different confine-

* qinxu@ust.hk

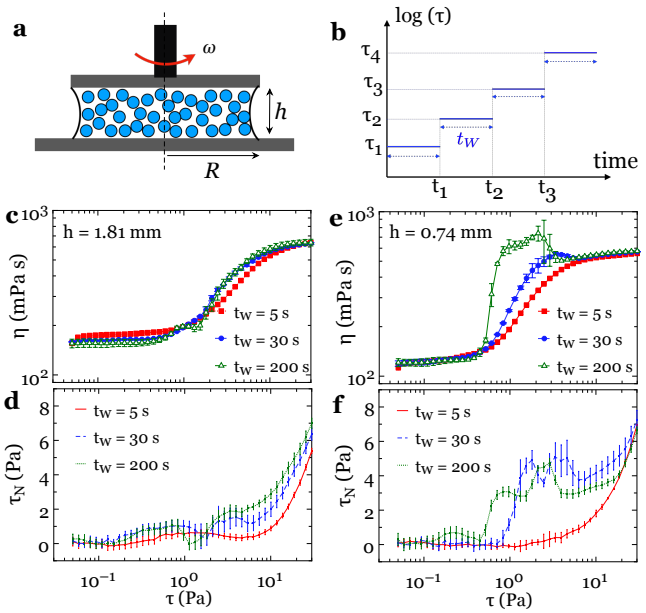

FIG. 1. **Shear rheology of the dense suspensions for different gap sizes.** **(a)** Schematic illustration of the parallel-plate shear cell used for measuring shear rheology. **(b)** Experimental protocol of characterizing the flow curves, where t_W is the time taken to measure each shear stress. **(c) & (d)** Plots of viscosity η (panel c) and normal stress τ_N (panel d) against shear stress τ for t_W = 5 s, 30 s, and 200 s with a fixed gap size h = 1.81 mm. **(e) & (f)** Plots of η (panel e) and τ_N (panel f) against τ with a reduced gap size h = 0.74 mm while t_W was varied from 5 s to 200 s. The error bars in the panels of (c)-(f) indicate the standard deviations from at least three repeated measurements. The particle volume fraction was kept at $\phi = 52\%$ in all the experiments.

ments (Fig. 1a). To minimize the uncertainties caused by sample-to-sample variations, each suspension was pre-sheared for at least 60 mins prior to measurements.

The rheology of glass-oil suspensions was characterized in stress-controlled approach with different gap sizes. For each flow curve, the shear stress τ was ramped up logarithmically with a sampling rate of 20 points per decade. As indicated by the schematic shown in Fig. 1b, we quantitatively controlled the duration of measurement (t_W) taken by the shear device at each shear stress (τ). The corresponding viscosity η was calculated as the ratio of τ and the average shear rate $\bar{\dot{\gamma}}$ over the period of t_W.

Figure 1c shows flow traces measured with a gap size of h = 1.81 mm for t_W = 5 s (red squares), 30 s (blue circles), and 200 s (green triangles), respectively. The suspension viscosity η increases monotonically with the shear stress τ, indicating a representative shear thickening behavior. The plots of $\eta(\tau)$ remain largely unchanged as t_W is varied. In the regimes of low ($\tau < 1$ Pa) and high shear stress ($\tau > 10$ Pa), we identified two distinctive Newtonian regimes, respectively, whose viscosities differed by a factor of four. The transition between the two regimes signifies a crossover from a lubricated to a frictional flow state [5]. The increase in suspension viscosity η is associated with an increase in the normal stress τ_N against the top shear plate. As shown in Fig. 1d, τ_N increases gradually within the range of 1 Pa $< \tau <$ 10 Pa, and then rises rapidly with τ in the frictional state ($\tau > 10$ Pa). The results indicate a continuous reinforcement of direct contacts between particles from the shear thickening onset ($\sim$ 1 Pa), which is a key rheological signature of a friction-dominated shear thickening transition in dense suspensions [11, 21].

To explore the role of boundary confinements in shear rheology, we next measured the flow curves of the same glass-oil suspensions ($\phi = 52\%$) but with a reduced gap size h = 0.74 mm. The resulting plots of $\eta(\tau)$ for different t_W (= 5 s, 30 s, 200 s) are shown in Fig. 1e. While the two distinct Newtonian regimes appear again at low (< 0.4 Pa) and high stress (> 4 Pa) regimes, respectively, the crossover between the two states varies markedly with t_W. As t_W increases from 5 s to 200 s, the flow curves of $\eta(\tau)$ become non-monotonic. At t_W = 200 s (the green triangles), there is a sharp increase in viscosity near an onset stress (≈ 0.4 Pa) until the suspension viscosity becomes $\eta \approx 7 \times 10^2$ mPa·s, even higher than that in the second Newtonian regime. As τ further increases beyond 2 Pa, η then decreases and returns back to 5×10^2 mPa·s. As no significant change in $\eta(\tau)$ was observed when t_W increased above 200 s (as later shown in Fig. 3b), we conclude that the non-monotonic flow curves represent a steady state behavior of confined suspensions.

This non-monotonic shear rheology is also associated with a different kind of normal stress response. Figure 1f shows the results of normal stress τ_N with an increasing shear stress τ for h = 0.74 mm. At t_W = 30 s (the blue dashed line) and 200 s (the green dotted line), we observed steep increases in τ_N as τ exceeds the thickening onset (≈ 0.4 Pa). Throughout the whole shear thickening regime (0.4 Pa $< \tau <$ 4 Pa), τ_N remained roughly constant around 4 Pa, substantially higher than that at h = 1.81 mm. Further increase of τ beyond the non-monotonic regime ($\tau > 4$ Pa) caused τ_N to continuously rise again.

III. *S*-SHAPED FLOW CURVES OF CONFINED SUSPENSIONS

We re-plotted the flow curves of the confined suspensions (h = 0.74 mm) as shear stress (τ) against shear rate ($\dot{\gamma}$) in Fig. 2a. The resulting plots of $\tau(\dot{\gamma})$ begin to bend towards the negative $\dot{\gamma}$ as the measuring time t_W increases. At t_W = 200 s, the flow curve (solid green line) displays a steady *S*-shaped profile, where a negative slope, $d\sigma/d\dot{\gamma} < 0$, appears between τ = 0.4 Pa and 0.8 Pa.

To further reveal the relationship between boundary confinements and non-monotonicity of flow curves, we systematically varied the gap size from h = 1.70 mm to 0.32 mm while keeping t_W = 200 s. The respective

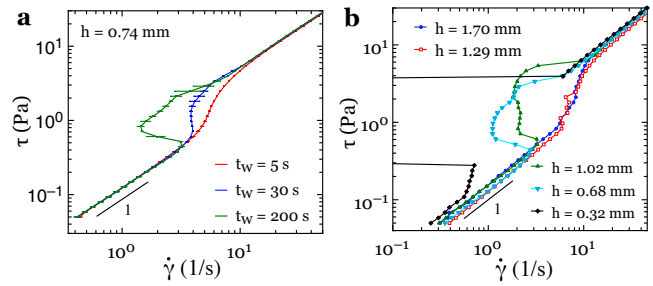

FIG. 2. ***S*-shaped flow curves. (a)** Plots of shear stress (τ) against shear rate ($\dot{\gamma}$) for t_W = 5 s, 30 s, and 200 s characterized at a constant gap size $h = 0.74$ mm. **(b)** Plots of $\tau(\dot{\gamma})$ with $t_W = 200$ s for different gap sizes, h =1.70 mm, 1.29 mm, 1.02 mm, 0.68 mm, and 0.32 mm, respectively.

plots of $\tau(\dot{\gamma})$ are shown in Fig. 2b. For $h = 1.70$ mm and 1.29 mm, shear stress τ increases monotonically with shear rate $\dot{\gamma}$. By contrast, non-monotonic S-shaped flow curves become visible at reduced gap sizes, $h = 1.02$ mm and 0.68 mm. As h further decreases to 0.32 mm, the plot of $\tau(\dot{\gamma})$ curves sharply towards $\dot{\gamma} \to 0$ at a critical stress $\tau_c = 0.3$ Pa. The suspension remained mostly static until passing a yield stress $\tau_y = 3.8$ Pa. Between τ_c and τ_y, the normal stress rises rapidly from τ_N =0.1 Pa to 50 Pa, implying a shear-jamming-like transition in the dense suspensions (see Appendix A). Since the particle size is about 43 μm, our results suggest that S-shaped flow curves begin to appear noticeable when the gap size becomes as small as ~ 25 particle diameters.

The results in Fig. 2 are in great contrast to previous studies on the rheology of dense non-Brownian suspensions. Recent experiments and simulations have revealed the coexistence of both frictional and lubricated flow states in strong shear thickening regimes [17, 18, 20]. The resulting flow behaviors destabilize shear profiles, and prevent non-monotonic rheological responses and shear jamming in unconfined suspensions [27]. Therefore, S-shaped flow curves have been rarely observed in steady state measurements [16]. Our results, however, suggest that these non-monotonic flow curves can be mechanically stabilized by confinements applied on shear boundaries to the dense suspensions.

IV. TEMPORAL FLUCTUATIONS OF GLOBAL SHEAR RATES

To search for the physical origin of the S-shaped flow curves, we next investigated the statistical properties of dense suspensions under different boundary confinements. Figure 3 summarizes how the global shear rate $\dot{\gamma}$ fluctuates over time t under constant shear stresses τ_a (= 1 Pa, 2 Pa, 3 Pa, 4 Pa, and 6 Pa) for two different gap sizes, $h = 1.68$ mm and $h = 0.87$ mm. For each τ_a, we measured the temporal evolution of $\dot{\gamma}(t)$ over a period of $T \sim 10^3$ s, such that the corresponding mean viscosity was defined as $\bar{\eta}(\tau_a) = \langle \tau_a/\dot{\gamma}(t) \rangle_T$. In panels (a) and (b), the resulting $\bar{\eta}(\tau_a)$ (the solid colored points) are plotted together with the reference flow curves $\eta_s(\tau)$ measured with $t_W = 5$ s (the black hollow points). Consistent with the rheological results in Fig. 1, $\bar{\eta}(\tau_a)$ greatly depends on the gap size. As shown in Fig. 3a, the $\bar{\eta}(\tau_a)$ values are nicely collapsed into the trace of $\eta_s(\tau)$, i.e., $\bar{\eta}(\tau_a) \approx \eta_s(\tau_a)$, suggesting no change in the flow curves with t_W for $h = 1.68$ mm. In contrast, for a reduced gap size $h = 0.87$ mm, $\bar{\eta}(\tau_a)$ is substantially larger than $\eta_s(\tau_a)$ from $\tau_a = 1$ Pa to 4 Pa in Fig. 3b. At $\tau_a = 6$ Pa, we found again that $\bar{\eta}(\tau_a) \approx \eta_s(\tau_a)$, indicating a non-monotonic flow curve. The plots of $\dot{\gamma}(t)$ at different τ_a are shown in panels (c) and (d), where the overall changes in $\dot{\gamma}(t)$ show similar dependence on τ_a for $h = 0.87$ mm and 1.68 mm. In both cases, their fluctuation amplitudes are maximized at $\tau_a = 2$ Pa and then quickly decrease with τ_a, and finally appear unnoticeable at $\tau_a = 6$ Pa.

We further calculated the standard deviation $\delta\dot{\gamma} = \overline{[(\dot{\gamma}(t) - \bar{\dot{\gamma}})^2]}^{1/2}$ for each $\dot{\gamma}(t)$ to quantify the intensity of fluctuations. Unexpectedly, as shown in Fig. 3e, $\delta\dot{\gamma}$ at $h = 1.68$ mm is larger than that at $h = 0.87$ mm between $\tau_a = 1$ Pa and 4 Pa. In previous experiments and simulations, shear fluctuations were commonly found to be amplified in non-monotonic flow regimes [20, 28, 29]. However, our experiments indicate the opposite results: the S-shaped flow curves $\tau(\dot{\gamma})$ (Fig. 3b) were associated with weakened fluctuations in global shear rate $\dot{\gamma}(t)$ (Fig. 3d) at a decreased gap size $h = 0.87$ mm. This counterintuitive statistical feature suggests that the governing flow mechanism of shear thickening in confined dense suspensions may become different.

V. LOCAL SHEAR STRESS OSCILLATIONS

To understand the relationship between flow behaviors and statistical properties in confined dense suspensions, we further looked into the flow heterogeneity developed during shear thickening transitions by using boundary stress microscopy (BSM). This technique was originally invented to measure tractions at soft interfaces [30, 31], and was recently improved for *in-situ* measurements of boundary shear stresses at fluid interfaces in rheological characterizations [32, 33]. In this work, to carry out BSM measurements, a 92-μm-thick layer of soft polydimethylsiloxane (PDMS) elastomer was coated onto a glass-bottomed plate. The whole shear cell was placed on top of a fluorescent microscope for *in-situ* imaging. The Young's modulus of the PDMS layer was chosen as $E = 1.7$ kPa to maintain an optimal resolution of boundary shear stresses. We deposited 1 μm fluorescent spheres at the PDMS surfaces as tracers to measure the in-plane deformations. By tracking the displacement fields of spheres ($\boldsymbol{u}$) under shear flows, we can locally resolve the shear stresses ($\boldsymbol{\sigma}$) at PDMS-flow interfaces based on the constitutive law for linear elastic solids,

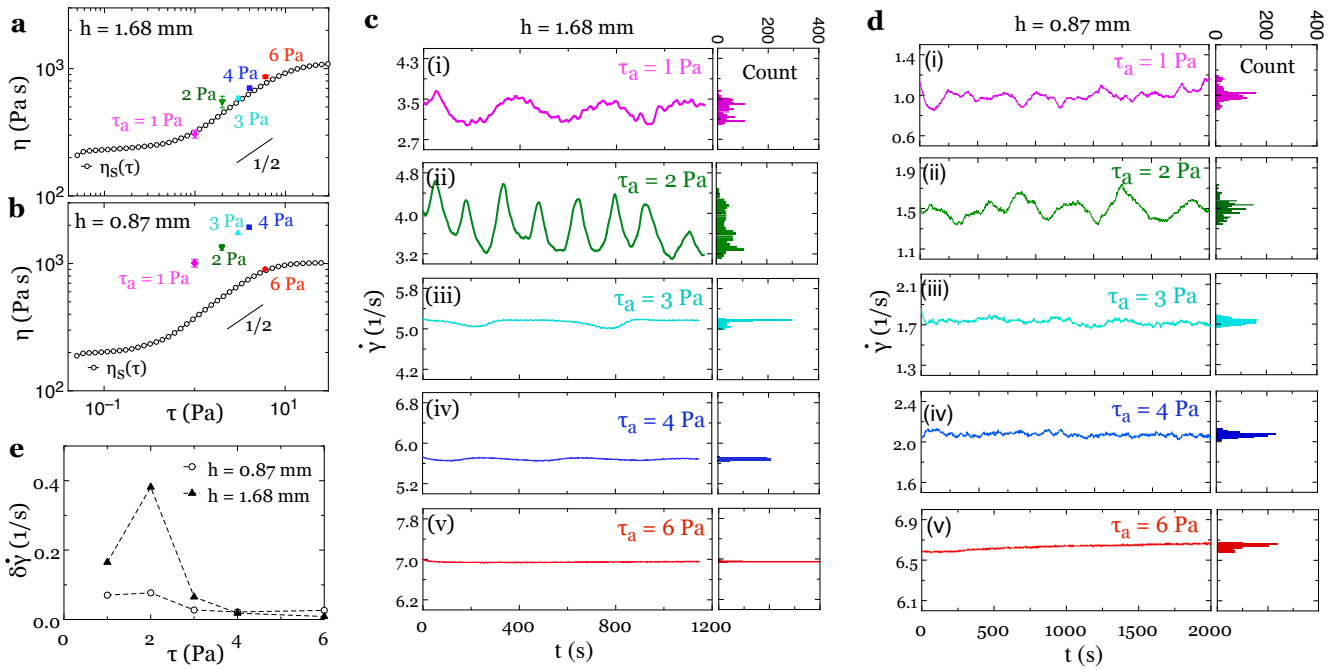

FIG. 3. **Temporal fluctuations of global shear rate. (a)** The black hollow circles represent the flow curves $\eta_s(\tau)$ measured with $t_W = 5$ s under a gap size $h = 1.68$ mm. The solid colored points indicate the mean viscosities ($\bar{\eta}$) measured at τ_a =1 Pa, 2 Pa, 3 Pa, 4 Pa, and 6 Pa over a period ($\sim 10^3$ s). **(b)** The black hollow circles represent the flow curves $\eta_s(\tau)$ measured with $t_W = 5$ s under a reduced gap size $h = 0.87$ mm. The solid colored points indicate $\bar{\eta}$ measured at the same τ_a in the confined suspension. The error bars in (a) and (b) are the standard deviations of $\bar{\eta}(\tau_a)$. **(c) & (d)** Temporal fluctuations of global shear rate $\dot{\gamma}(t)$ measured for $h = 0.87$ mm and $h = 1.68$ mm, respectively. The sub-panels (i) to (v) in each column of images show the temporal evolution of $\dot{\gamma}(t)$ under the constant shear stresses τ_a =1 Pa, 2 Pa, 3 Pa, 4 Pa, and 6 Pa, respectively. **(e)** Plots of $\delta\dot{\gamma}$ against τ_a for both $h = 0.87$ mm and $h = 1.68$ mm.

$$\boldsymbol{\sigma} = \frac{E}{1+\nu}\left(\frac{1}{2}(\nabla \boldsymbol{u} + \nabla \boldsymbol{u}^T) + \frac{\nu \nabla \cdot \boldsymbol{u}}{1-2\nu}\boldsymbol{I}\right), \qquad (1)$$

and the mechanical equilibrium requirement $\nabla \cdot \boldsymbol{\sigma} = 0$, or

$$(1-2\nu)\nabla^2 \boldsymbol{u} + \nabla(\nabla \cdot \boldsymbol{u}) = 0. \qquad (2)$$

Here E and ν are the Young's modulus and the Poisson ratio of the PDMS substrate while $\boldsymbol{I}$ is the identity tensor. The numerical method to solve Eqs. 1 and 2 for BSM experiments can be found in [34]. From our previous study [35], we have characterized that the Poisson ratio of this coated PDMS material is $\nu = 0.48$.

Prior to rheo-optical experiments, we have systematically calibrated our imaging system to ensure a high resolution of measured boundary stresses. For the shear plate with a radius of R, the microscope objective was kept at a distance of $2R/3$ from the plate center so that the local shear rate was identical to the global shear rate ($\dot{\gamma}$). The subscripts x and y were used to denote the flow direction and vorticity direction, respectively. In all the experiments, we have found that the boundary stress in the flow direction remained much higher than that in the vorticity direction, $\sigma_x \gg \sigma_y$. Therefore, we exclusively focused on the spatiotemporal fluctuations of σ_x to examine the flow heterogeneity. The detailed experimental protocol of performing boundary stress microscopy is discussed in Appendix B.

Figure 4 summarizes the evolution of σ_x over time for a reduced gap size $h = 0.87$ mm. We denoted as $\langle\sigma_x\rangle$ the spatially averaged stress within a field of view (880 μm $\times$ 660 μm). Panel (a) presents the plots of $\langle\sigma_x\rangle$ against time t at different global shear stresses τ_a, and panel (b) shows the zoom plots of $\langle\sigma_x(t)\rangle$ from the duration between t = 200 s to 400 s. Within the non-monotonic regime, from $\tau_a = 1$ Pa to 4 Pa, $\langle\sigma_x(t)\rangle$ fluctuates significantly between a dominating low-stress state and a series of high-stress peaks. While the low-stress regimes remain close to zero, the peak stresses of $\langle\sigma_x(t)\rangle$ approximately doubles, from 15 Pa to 30 Pa, as τ_a increases from 1 Pa to 4 Pa. Panels (c) and (d) in Fig. 4 show the representative stress maps of σ_x measured by BSM at different time points for τ_a = 1 and 3 Pa, respectively (see the Supplemental Video S1 and S2). The exchange between the two different stress states suggests that a spatial phase separation occurred during shear thickening transitions [33]. The high-stress domains were concentrated in a small area fraction of suspensions while the majority of the suspension areas bore minimal stresses.

As the global shear stress further increased to τ_a =

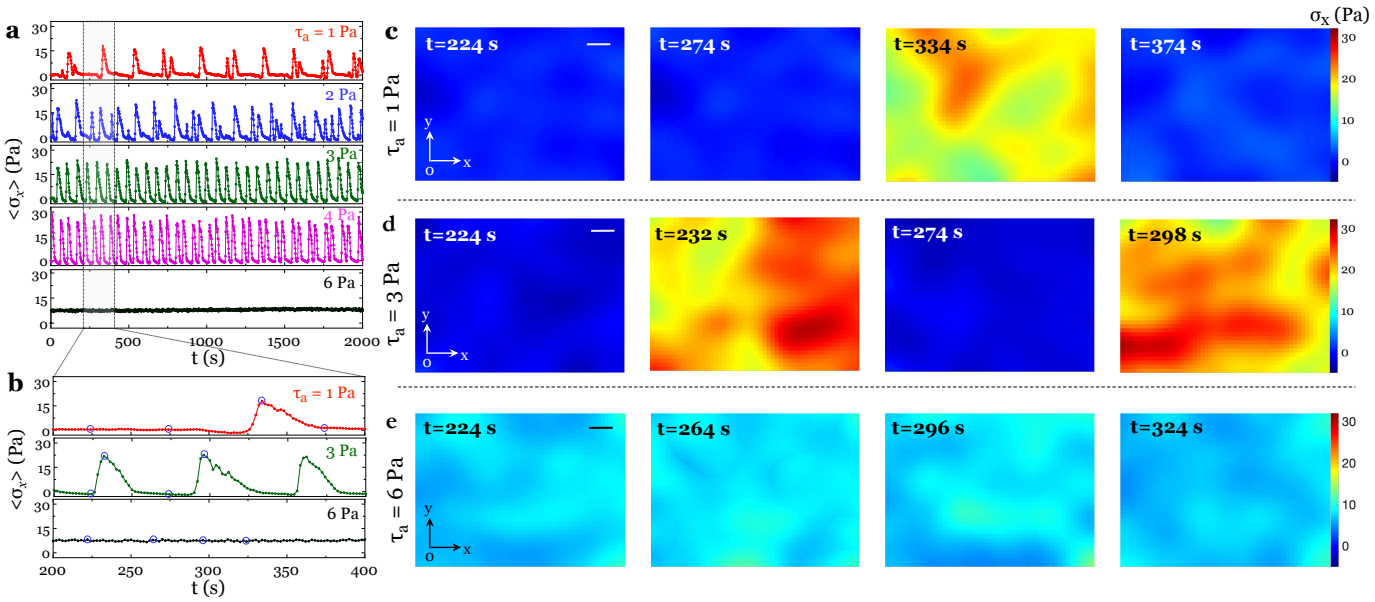

FIG. 4. **Local stress oscillation in confined suspensions**. **(a)** Temporal fluctuations of the average local shear stresses, $\langle\sigma_x(t)\rangle$, measured at different global shear stresses (τ_a). From top to bottom, $\tau_a = 1$ Pa, 2 Pa, 3 Pa, 4 Pa, and 6 Pa, respectively. **(b)** Zoom plots of $\langle\sigma_x(t)\rangle$ at $\tau_a = 1$ Pa, 3 Pa, and 6 Pa from the duration between $t = 200$ s and 400 s. The blue circles indicate the specific time points where the associated local stress maps σ_x are shown in panels (c) to (e). **(c)** Snapshots of the local stress maps (σ_x) at the time points, $t = 224$ s, 274 s, 334 s, and 374 s, for $\tau_a = 1$ Pa. **(d)** Snapshots of the local stress maps (σ_x) at the time points, $t = 224$ s, 232 s, 274 s, 298 s, for $\tau_a = 3$ Pa. **(e)** Snapshots of the local stress maps (σ_x) at the time points, $t = 224$ s, 264 s, 296 s, and 324 s, for $\tau_a = 6$ Pa. Scale bars: 100 μm.

6 Pa, spatial stress heterogeneity notably decreased. This mitigation of local stress oscillations can be seen in both of the black line in Fig. 4a and the stress maps in Fig. 4e. At $\tau_a = 6$ Pa, σ_x remains approximately constant (~ 7.8 Pa) across the field of view (see the Supplemental Video S3). We interpret the the homogenization of shear flows as a dynamic yielding process. The high-stress regions above the local yield stress quickly relaxed under shear, such that the spatial phase separation disappeared. On macroscopic scales, the flow homogenization at $\tau_a = 6$ Pa led to a reduced flow resistance and thus generated non-monotonic flow curves.

To quantify the timescales (t_c) of the observed local stress oscillations, we calculated the autocorrelation functions of $\langle\sigma_x(t)\rangle$ across a measurement period T by using the formula

$$R_x(\delta t) = \frac{\int_0^T \langle\sigma_x(t)\rangle\langle\sigma_x(t+\delta t)\rangle dt}{\int_0^T [\langle\sigma_x(t)\rangle]^2 dt} \qquad (3)$$

where δt denotes a given time shift. When $\delta t \approx t_c$, we expect local maximums in the plots of $R_x(\delta t)$. Figure 5a represents the results of $R_x(\delta t)$ calculated for $\tau_a = 1$ Pa, 3 Pa, and 4 Pa, respectively, and Fig. 5b displays the zoom plots of the corresponding $\langle\sigma_x(t)\rangle$. The peaks of $R_x(\delta t)$ are consistent with the characteristic oscillation timescales of $\langle\sigma_x(t)\rangle$. When $\tau_a = 1$ Pa, the first peak in $R_x(\delta t)$ is located at $\delta t_p = 192$ s, which nicely approximates the time interval between two adjacent peaks (t_{c1}) in the top panel of Fig. 5b.

As shear stress increased to $\tau_a = 3$ Pa and 4 Pa, $\langle\sigma_x(t)\rangle$ oscillated more rapidly, and involves two distinct timescales in $R_x(\delta t)$. For example, we observed a first local maximum of $R_x(\delta t)$ at $\delta t_s = 62$ s followed by a major peak at $\delta t_p = 106$ s for $\tau_a = 4$ Pa. The longer timescale ($t_{c1} \approx \delta t_p = 106$ s) corresponds to the intervals between two major peaks in the plot of $\langle\sigma_x(t)\rangle$, while the shorter timescale ($t_{c2} \approx \delta t_s = 62$ s) approximates a sub-interval between a lower spike and a major peak. The two intervals are indicated by the black and pink arrows in Fig. 5b.

We further compared both t_{c1} and t_{c2} with the rotational period of the shear plate, $T_g = 4\pi R/(3\dot{\gamma}h)$. Figure 5c exhibits the plots of both t_{c1} and t_{c2} against different T_g. For $\tau_a = 1$ Pa and 2 Pa, only one timescale (t_{c1}) was measured by the autocorrelation analysis. Based on the relationship between $t_{c1,2}$ and T_g, we found two generic linear scalings,

$$t_{c1} \approx 2T_g \ , \qquad t_{c2} \approx T_g. \qquad (4)$$

The dependence of t_{c1} and t_{c2} on T_g suggests a physical picture that potentially delineates the dynamic stress separations in confined suspensions. When $\tau_a = 1$ Pa or 2 Pa, briefly exceeding the shear thickening onset initiated a high-stress domain to form in the shear flow. If its center of mass was located at a height approximately half of the gap size [24], the mean traveling speed of the high-stress domain was approximately half of the shear plate. As a result, the high-stress region finished one

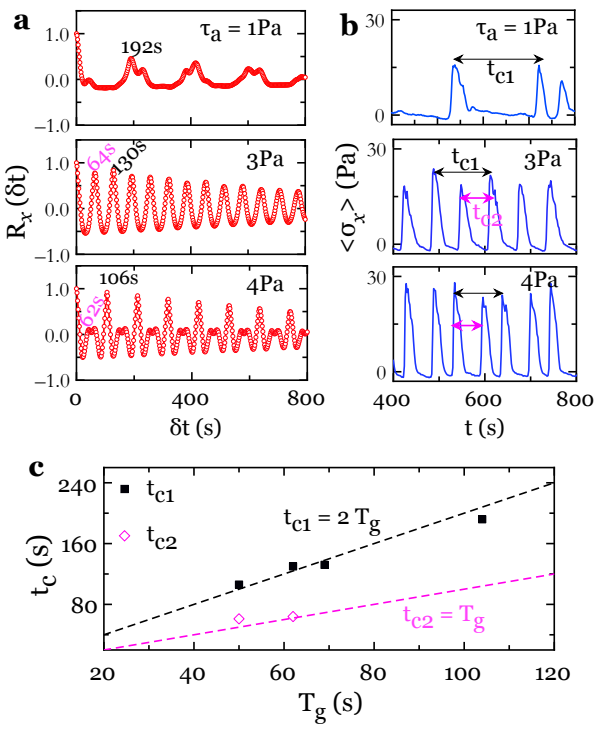

FIG. 5. **Oscillation timescales of local shear stress σ_x in confined suspensions ($h = 0.87$ mm).** **(a)** Autocorrelation functions $R_x(\delta t)$ at different global shear stresses, $\tau_a = 1$ Pa, 3 Pa, and 4 Pa, respectively. **(b)** Zoom plots of $\langle\sigma_x\rangle$ against t at $\tau_a = 1$ Pa, 3 Pa, and 4 Pa. The two characteristic timescales, t_{c1} and t_{c2}, are indicated by the black and pink arrows. **(c)** Plots of t_{c1} and t_{c2} against the rotational period of shear plate T_g.

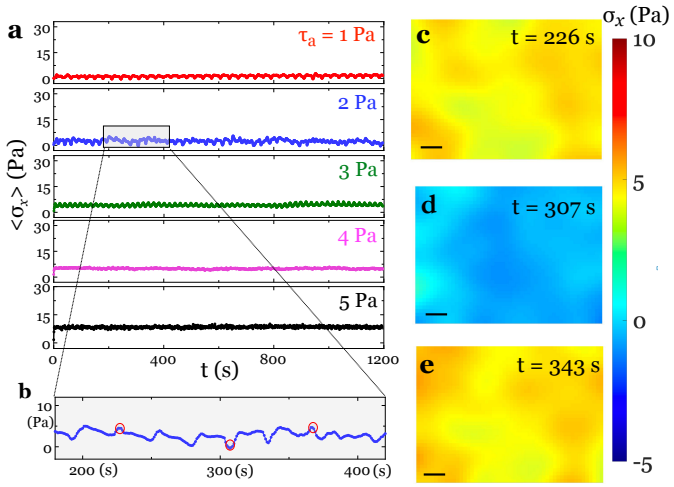

FIG. 6. **Fluctuations of local shear stress σ_x under a large gap size $h = 1.68$ mm.** **(a)** Plots of $\langle\sigma_x(t)\rangle$ at different global shear stresses τ_a. From top to bottom, $\tau_a = 1$ Pa, 2 Pa, 3 Pa, 4 Pa, and 6 Pa, respectively. **(b)** Zoom plots of $\langle\sigma_x(t)\rangle$ at $\tau_a = 2$ Pa. The red circles denote the specific time points, $t = 226$ s, 307 s, and 343 s. **(c) - (e)** Local stress maps of σ_x measured at the time points, $t = 226$ s, 307 s, 343 s, with a constant global shear stress $\tau_a = 2$ Pa. Scale bars: 100 μm.

complete round while the shear plate rotated two periods, $t_{c1} \approx 2T_g$. When shear stress increased to $\tau_a = 3$ Pa or 4 Pa, a second high-stress domain appeared in a different location within the suspension. Therefore, we observed the high-stress regions twice as frequently as we did at lower stresses, such that $t_{c2} \approx T_g$. Although we expected more high-stress regions to appear with an increasing global shear stress τ_a, we experimentally found yielding and homogenization across the whole shear flows at $\tau_a = 6$ Pa.

Finally, to confirm the role of boundary confinements in stress separations, we also measured the spatiotemporal evolution of local shear stresses under a large gap size, $h = 1.68$ mm. Figure 6a presents the plots of $\langle\sigma_x(t)\rangle$ at different τ_a. As shown in Appendix C, a characteristic oscillation time scale $t_{c1} \approx 2T_g$ was again identified through autocorrelation analysis. However, the fluctuations of $\langle\sigma_x(t)\rangle$ reduced substantially compared with that of confined suspensions. For example, as h increased from 0.87 mm to 1.68 mm, the fluctuation amplitudes of $\langle\sigma_x(t)\rangle$ declined from 20 Pa to 5 Pa at $\tau_a = 2$ Pa. Panels (c) to (e) in Fig. 6 show the stress maps of σ_x measured at different time points ($t = 226$ s, 307 s, and 343 s) for $\tau_a = 2$ Pa (see the Supplemental Video S4) where the stress heterogeneity also weakens substantially at $h = 1.68$ mm. These results confirm that the apparent local stress separation shown in Fig. 4 was indeed initiated by boundary confinements.

VI. DISCUSSIONS AND CONCLUSIONS

Our results have shown that boundary confinements change the underlying flow structures during shear thickening transitions. Both the rheological and statistical properties of dense suspensions are varied across different length scales. To clarify the shear thickening mechanism in confined conditions, we now discuss the physical significance of several important observations in our experiments.

First, we consider the relationship between the fluctuations of global shear rate $\dot{\gamma}$ and local shear stress $\langle\sigma_x\rangle$ in stress-controlled rheological measurements. It has been previously assumed that strong shear thickening flows, including that in non-monotonic regimes, were often associated with rapid growth and relaxation of disordered contact networks spanning whole suspensions. Therefore, enhanced temporal fluctuations and spatial heterogeneities of shear flows were both found during shear thickening transitions [17, 25, 36]. However, the relationship between temporal and spatial fluctuations of shear thickening fluids has not yet been explored. In the non-monotonic flow regimes of confined suspensions, we measured enhanced oscillations of local shear stress $\langle\sigma_x\rangle$ (Fig. 4) but with simultaneously reduced fluctuations of

global shear rate $\dot{\gamma}$ (Fig. 3).

We interpret the experimental findings as indicating that global fluctuations in shear rate ($\dot{\gamma}$) and local stress separations (σ_x) are two competing mechanisms that arise in response to a constant global shear stress during shear thickening transition. Macroscopically, $\dot{\gamma}$ can fluctuate over time to maintain a constant global shear stress through a dynamically evolving force network. Locally, suspensions under a constant global shear stress can separate into regions bearing different σ_x, including a ubiquitous low-stress domain and several concentrated high-stress clusters.

The governing statistical features in response to shear thickening will depend on how confined suspensions are. In a weakly confined suspension (e.g., $h = 1.68$ mm), as the correlation length of particle interactions remains smaller than the system size, any high-stress domains that form will become mechanically unstable and relax rapidly in shear flows [17]. As a result, dense suspensions remain spatially homogeneous. In these scenarios, a constant shear stress is maintained by the fluctuations of global shear rate $\dot{\gamma}$, which are the dominating statistical features [28]. By contrast, in highly confined suspensions (e.g., $h = 0.87$ mm), local stress separations can sustain and steadily travel along shear flows. These formations of local high-stress domains help to maintain a constant global shear stress (τ_a). Therefore, the global shear rate ($\dot{\gamma}$) oscillates less significantly even in the non-monotonic flow regimes of confined suspensions (Fig. 3).

Second, it is worth to mention again that S-shaped curves have been challenging to directly measure in steady state due to the disruptions by various flow instabilities [27, 37]. However, our experiments show that confinement-induced separations of local shear stresses (σ_x) were spatiotemporally stable during shear thickening transitions. As the global shear stress increases, the growth and yielding of these local high-stress domains result in the steady non-monotonic flow curves (Figs. 1 and 2).

In summary, we present a systematic study that reveals the underlying connection between shear thickening rheology and flow fluctuations in confined dense suspensions. Specifically, we have shown that the confinement applied by shear boundaries can effectively induce stress heterogeneity that controls shear thickening flows on different length scales. Globally, the flow curves become non-monotonic, or S-shaped. Locally, we identified sustained stress oscillations. We anticipate that the work can bring valuable insight into dynamic control of suspension rheology through pre-designed boundary effects.

VII. ACKNOWLEGDEMENT

We thank Dr. Endao Han, Prof. Yilong Han, Prof. Jidong Zhao, and Prof. Yifan Wang for their valuable suggestions. This work was supported by the General Research Funds (No. 16307422 and No. 16305821) from the Hong Kong Research Grants Council and the Partnership Seed Fund (No. ASPIRE2021#1) from the Asian Science and Technology Pioneering Institutes of Research and Education League.

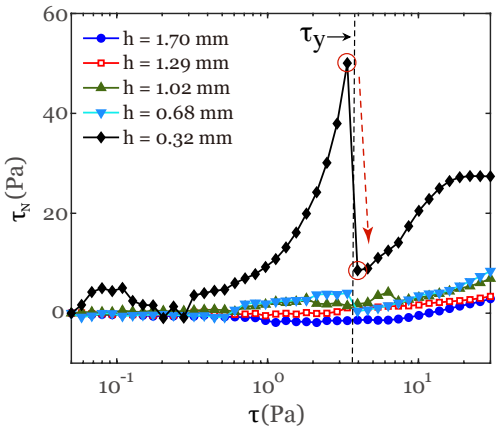

FIG. 7. **Normal stress measurements.** Plots of normal stress (τ_N) against shear stress (τ) at various gap sizes, $h = 1.70$ mm, 1.29 mm, 1.02 mm, 0.68 mm, and 0.32 mm, respectively. The time taken for measuring each data point maintained at $t_W = 200$ s. The black dashed line indicates the yield stress τ_y.

Appendix A: Normal Stress Measurements

During the rheological characterizations, we simultaneously measured the normal stress τ_N applied to the shear plate under different confinement conditions. Figure 7 plots normal stress τ_N against shear stress τ with different gap sizes (h). For $h = 0.68$ mm or larger, τ_N remains in the order of 10^0 Pa. In contrast, for the smallest gap size $h = 0.32$ mm, the normal stress rises rapidly to 50 Pa near the yield stress $\tau_y \approx 3.8$ Pa (see the black diamonds). Upon further increasing shear stress beyond τ_y, τ_N suddenly drops to 8.6 Pa, and then gradually increases again with an approximate linear scaling, $\tau_N \sim 2\tau$. For $h = 0.32$ mm, the rapid growth and collapse of τ_N near the yield stress τ_y indicate a shear-jamming-like transition followed by a rapid relaxation process in this extremely confined suspension. The return to a positive relationship between τ_N and shear stress τ above τ_y is the rheological signature of a frictional flow state [11, 21].

Appendix B: Boundary Stress Microscopy

To realize *in-situ* boundary stress microscopy (BSM) in our rheological measurements, a thin elastic polydimethylsiloxane (PDMS) substrate was coated on the bottom shear plate. First, we fully mixed a silicone base solution (divinyl-terminated polydimethylsiloxane, DMS-V31, Gelest Inc.) with 0.8 wt% crosslinkers (a

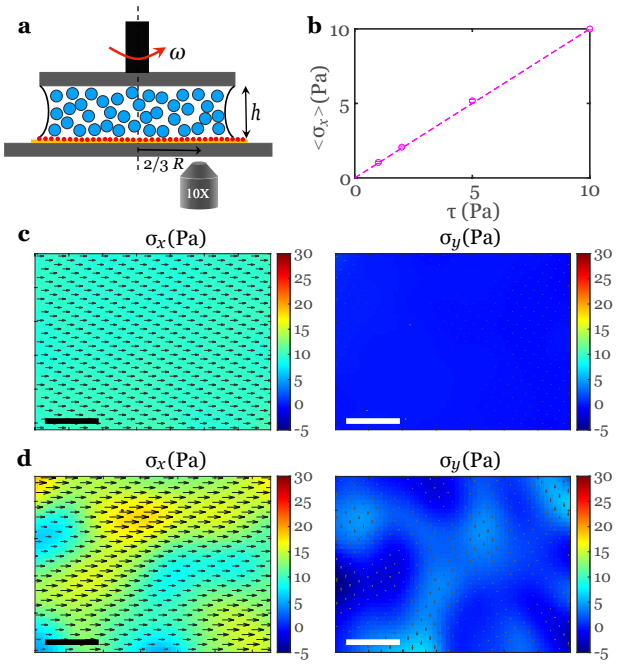

FIG. 8. **Boundary stress microscopy. (a)** Schematic illustration of our BSM setup. Fluorescent microspheres attached to the PDMS are indicated by the red dots. **(b)** The calibrated local shear stress $\langle\sigma_x\rangle$ is plotted against global shear stress τ for 100 cSt silicone oil. The dashed line indicates the scaling $\langle\sigma_x\rangle = \tau$. **(c)** Boundary stresses σ_x and σ_y measured at $\tau_a = 10$ Pa for 100 cSt silicone oil. **(d)** Boundary stresses σ_x and σ_y measured at $\tau_a = 3$ Pa for dense suspensions with a confined gap size $h = 0.87$ mm. The arrows in panels (c) and (d) indicate the displacement fields. Scale bars: 200 μm.

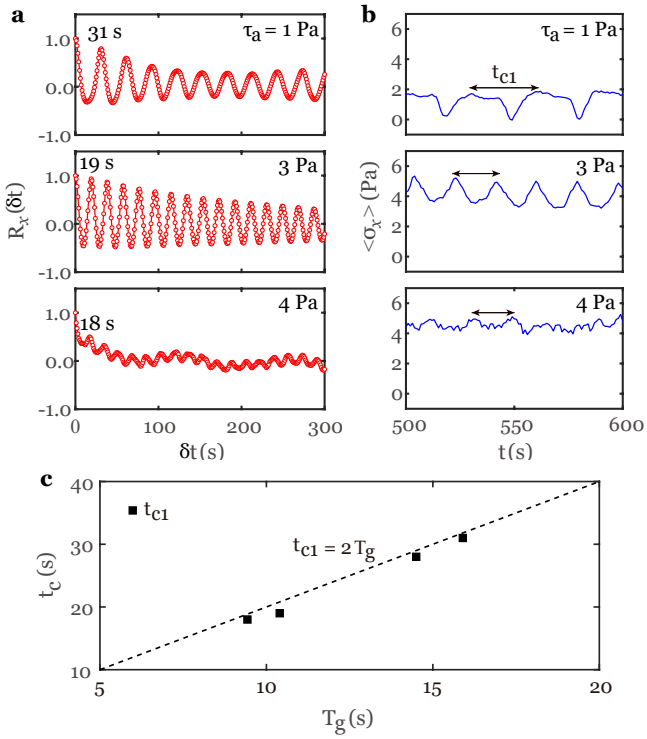

FIG. 9. **Local stress oscillations in weakly confined suspensions. (a)** Autocorrelation function $R_x(\delta t)$ of $\langle\sigma_x(t)\rangle$ under different global shear stresses, $\tau_a = 1$ Pa, 3 Pa, and 4 Pa, respectively. **(b)** Zoom plots of $\langle\sigma_x(t)\rangle$ from Fig. 6a. The black arrows indicate the characteristic oscillation timescale t_{c1}. **(c)** The oscillation timescale of local shear stresses t_{c1} is plotted against the global shear period T_g.

trimethylsiloxane terminated-dimethylsiloxane copolymer, HMS-301, Gelest Inc.) and 0.01 wt% catalyst (a platinum-divinyltetramethyldisiloxane complex in xylene, SIP6831.2, Gelest Inc.). After being degassed, the mixture solution was spin-coated onto the bottom glass plate at a speed of 800 rpm for 3 minutes and then cured at 40 °C for 48 hours. To avoid swelling effects induced by the solvent in suspensions, the cured PDMS substrate was pre-swelled in 20 cSt silicone oil prior to BSM measurements. As a result, the thickness of a fully swollen PDMS substrate was 92 μm.

To measure the in-plane deformations of PDMS surfaces, we attached a layer of 1 μm carboxylate-modified fluorescent beads (excitation/emission at 535/575 nm) onto the PDMS-suspension interface. The entire shear cell was placed on top of a fluorescent microscope equipped with a 10× objective to image the movements of beads. Using a tracking algorithm for particles with large displacements [38], we determined the displacement fields $\boldsymbol{u}$ of the fluorescent beads. A gradual drift of the microscope objective along the vertical direction was found to affect the accuracy of the displacement measurements. To minimize this effect, we waited for at least 12 hours after positioning the objective at an initial position before making measurements. As a result, the displacement of fluorescent beads caused by further drift of the microscope objective was less than 0.03 μm during the period of each measurement. The resulting stress uncertainty was in the order of 0.2 Pa, which was much smaller than the local stresses of interest.

To determine the Young's modulus E of a swollen PDMS substrate, we experimentally calibrated our rheo-optical system by using a standard 100 cSt silicone oil. To ensure that the local shear stress $\langle\sigma_x\rangle$ measured by BSM was consistent with the applied shear stress τ for the testing silicone oil, we fitted the Young's modulus as $E = 1.7$ kPa. Figure 8b shows the plot of $\langle\sigma_x\rangle$ against τ measured for 100 cSt silicone oil where the dashed line indicates the linear scaling, $\langle\sigma_x\rangle = \tau$.

In our rheo-optical measurements, BSM characterized the shear stresses in both the flow direction (σ_x) and vorticity direction (σ_y). Panels (c) and (d) in Fig. 8 show representative local stresses (σ_x and σ_y) measured for a pure silicone oil (100 cSt) and a highly confined suspension ($h = 0.87$ mm), respectively. In both cases, the magnitudes of σ_y are negligible compared with that of σ_x (see the Supplemental Video S5). We thus exclusively focused on the spatial heterogeneity of σ_x in our studies.

Appendix C: Local Stress Oscillations in Weakly Confined Suspensions

In weakly confined suspensions, we show that only one characteristic timescale can be identified through autocorrelation analysis (Eq. 3). For instance, Fig. 9a represents the results of $R_x(\delta t)$ at different τ_a for $h = 1.68$ mm. The peaks of $R_x(\delta t)$ are highly consistent with the characteristic fluctuation timescales t_{c1} in Fig. 9b. Compared with the global rotational period T_g, t_{c1} also follows the same linear scaling as that in confined suspensions (Fig. 9c),

$$t_{c1} \approx 2T_g. \tag{C1}$$

However, there was no well-defined second timescale t_{c2} for any of the applied stresses.

[1] Fabio Vittorio De Blasio, "Rheology of a wet, fragmenting granular flow and the riddle of the anomalous friction of large rock avalanches," Granular Matter **11**, 179 (2009).

[2] Abhay Goyal, Ivan Palaia, Katerina Ioannidou, Franz-Josef Ulm, Henri van Damme, Roland J.-M. Pellenq, Emmanuel Trizac, and Emanuela Del Gado, "The physics of cement cohesion," Science Advances **7**, eabg5882 (2021).

[3] Juan de Vicente, Daniel J. Klingenberg, and Roque Hidalgo-Alvarez, "Magnetorheological fluids: a review," Soft Matter **7**, 3701–3710 (2011).

[4] Wing Yim Tam, Guang Hua Yi, Weijia Wen, Hongru Ma, M. M. T. Loy, and Ping Sheng, "New electrorheological fluid: Theory and experiment," Phys. Rev. Lett. **78**, 2987–2990 (1997).

[5] Jeffrey F. Morris, "Shear thickening of concentrated suspensions: Recent developments and relation to other phenomena," Annual Review of Fluid Mechanics **52**, 121–144 (2020).

[6] Eric Brown and Heinrich M Jaeger, "Shear thickening in concentrated suspensions: phenomenology, mechanisms and relations to jamming," Reports on Progress in Physics **77**, 046602 (2014).

[7] Christopher Ness, Ryohei Seto, and Romain Mari, "The physics of dense suspensions," Annual Review of Condensed Matter Physics **13**, 97–117 (2022).

[8] M. Wyart and M. E. Cates, "Discontinuous shear thickening without inertia in dense non-brownian suspensions," Phys. Rev. Lett. **112**, 098302 (2014).

[9] Romain Mari, Ryohei Seto, Jeffrey F. Morris, and Morton M. Denn, "Discontinuous shear thickening in brownian suspensions by dynamic simulation," Proceedings of the National Academy of Sciences **112**, 15326–15330 (2015).

[10] B. M. Guy, M. Hermes, and W. C. K. Poon, "Towards a unified description of the rheology of hard-particle suspensions," Phys. Rev. Lett. **115**, 088304 (2015).

[11] John R. Royer, Daniel L. Blair, and Steven D. Hudson, "Rheological signature of frictional interactions in shear thickening suspensions," Phys. Rev. Lett. **116**, 188301 (2016).

[12] Nayoung Park, Vikram Rathee, Daniel L. Blair, and Jacinta C. Conrad, "Contact networks enhance shear thickening in attractive colloid-polymer mixtures," Phys. Rev. Lett. **122**, 228003 (2019).

[13] Romain Mari and Ryohei Seto, "Force transmission and the order parameter of shear thickening," Soft Matter **15**, 6650–6659 (2019).

[14] Shravan Pradeep, Mohammad Nabizadeh, Alan R. Jacob, Safa Jamali, and Lilian C. Hsiao, "Jamming distance dictates colloidal shear thickening," Phys. Rev. Lett. **127**, 158002 (2021).

[15] Romain Mari, Ryohei Seto, Jeffrey F. Morris, and Morton M. Denn, "Nonmonotonic flow curves of shear thickening suspensions," Phys. Rev. E **91**, 052302 (2015).

[16] Zhongcheng Pan, Henri de Cagny, Bart Weber, and Daniel Bonn, "S-shaped flow curves of shear thickening suspensions: Direct observation of frictional rheology," Phys. Rev. E **92**, 032202 (2015).

[17] Qin Xu, Abhinendra Singh, and Heinrich M. Jaeger, "Stress fluctuations and shear thickening in dense granular suspensions," Journal of Rheology **64**, 321–328 (2020).

[18] Rijan Maharjan, Ethan O'Reilly, Thomas Postiglione, Nikita Klimenko, and Eric Brown, "Relation between dilation and stress fluctuations in discontinuous shear thickening suspensions," Phys. Rev. E **103**, 012603 (2021).

[19] Didier Lootens, Henri Van Damme, and Pascal Hébraud, "Giant stress fluctuations at the jamming transition," Phys. Rev. Lett. **90**, 178301 (2003).

[20] Omer Sedes, Abhinendra Singh, and Jeffrey F. Morris, "Fluctuations at the onset of discontinuous shear thickening in a suspension," Journal of Rheology **64**, 309–319 (2020).

[21] Eric Brown and Heinrich M. Jaeger, "The role of dilation and confining stresses in shear thickening of dense suspensions," Journal of Rheology **56**, 875–923 (2012).

[22] Qin Xu, Sayantan Majumdar, Eric Brown, and Heinrich M. Jaeger, "Shear thickening in highly viscous granular suspensions," Europhysics Letters **107**, 68004 (2014).

[23] Ryohei Seto and Giulio G. Giusteri, "Normal stress differences in dense suspensions," Journal of Fluid Mechanics **857**, 200–215 (2018).

[24] Guillaume Ovarlez, Anh Vu Nguyen Le, Wilbert J. Smit, Abdoulaye Fall, Romain Mari, Guillaume Chatté, and Annie Colin, "Density waves in shear-thickening suspensions," Science Advances **6**, eaay5589 (2020).

[25] Brice Saint-Michel, Thomas Gibaud, and Sébastien Manneville, "Uncovering instabilities in the spatiotemporal dynamics of a shear-thickening cornstarch suspension," Phys. Rev. X **8**, 031006 (2018).

[26] Abdoulaye Fall, Anaël Lemaître, Fran çois Bertrand, Daniel Bonn, and Guillaume Ovarlez, "Shear thickening and migration in granular suspensions," Phys. Rev. Lett. **105**, 268303 (2010).

[27] Endao Han, Nicole M. James, and Heinrich M. Jaeger, "Stress controlled rheology of dense suspensions using transient flows," Phys. Rev. Lett. **123**, 248002 (2019).

[28] Michiel Hermes, Ben M. Guy, Wilson C. K. Poon, Guilhem Poy, Michael E. Cates, and Matthieu Wyart, "Unsteady flow and particle migration in dense, non-brownian suspensions," Journal of Rheology **60**, 905–916 (2016).

[29] Takeshi Kawasaki and Ludovic Berthier, "Discontinuous shear thickening in brownian suspensions," Phys. Rev. E **98**, 012609 (2018).

[30] Ye Xu, Wilfried C. Engl, Elizabeth R. Jerison, Kevin J. Wallenstein, Callen Hyland, Larry A. Wilen, and Eric R. Dufresne, "Imaging in-plane and normal stresses near an interface crack using traction force microscopy," Proceedings of the National Academy of Sciences **107**, 14964–14967 (2010).

[31] Aaron F. Mertz, Shiladitya Banerjee, Yonglu Che, Guy K. German, Ye Xu, Callen Hyland, M. Cristina Marchetti, Valerie Horsley, and Eric R. Dufresne, "Scaling of traction forces with the size of cohesive cell colonies," Phys. Rev. Lett. **108**, 198101 (2012).

[32] Vikram Rathee, Daniel L. Blair, and Jeffrey S. Urbach, "Localized stress fluctuations drive shear thickening in dense suspensions," Proceedings of the National Academy of Sciences **114**, 8740–8745 (2017).

[33] Vikram Rathee, Daniel L. Blair, and Jeffrey S. Urbach, "Localized transient jamming in discontinuous shear thickening," Journal of Rheology **64**, 299–308 (2020).

[34] Robert W Style, Rostislav Boltyanskiy, Guy K German, Callen Hyland, Christopher W MacMinn, Aaron F Mertz, Larry A Wilen, Ye Xu, and Eric R Dufresne, "Traction force microscopy in physics and biology," Soft matter **10**, 4047–4055 (2014).

[35] Qin Xu, Lawrence A. Wilen, Katharine E. Jensen, Robert W. Style, and Eric R. Dufresne, "Viscoelastic and poroelastic relaxations of soft solid surfaces," Phys. Rev. Lett. **125**, 238002 (2020).

[36] Lance E. Edens, Sidhant Pednekar, Jeffrey F. Morris, Gregory K. Schenter, Aurora E. Clark, and Jaehun Chun, "Global topology of contact force networks: Insight into shear thickening suspensions," Phys. Rev. E **99**, 012607 (2019).

[37] Peter D. Olmsted, "Perspectives on shear banding in complex fluids," Rheologica Acta **47**, 283–300 (2008).

[38] Rostislav Boltyanskiy, Jason W. Merrill, and Eric R. Dufresne, "Tracking particles with large displacements using energy minimization," Soft Matter **13**, 2201–2206 (2017).